forests

MDPI

Article

Aboveground Biomass Retrieval in Tropical and Boreal Forests Using L-Band Airborne Polarimetric Observations

Mengjin Wang [1], Wangfei Zhang [1,*], Yongjie Ji [2], Armando Marino [3], Kunpeng Xu [4], Lei Zhao [4], Jianmin Shi [1] and Han Zhao [1]

[1] College of Forestry, Southwest Forestry University, Kunming 650224, China; wmj@swfu.edu.cn (M.W.); zhan98gisrs@swfu.edu.cn (H.Z.)
[2] School of Geography and Ecotourism, Southwest Forestry University, Kunming 650224, China
[3] Biological and Environmental Sciences, The University of Stirling, Stirling FK9 4LA, UK
[4] Institute of Forest Resources Information Technique, Chinese Academy of Forestry, Beijing 100091, China
* Correspondence: mewhff@163.com

Abstract: Forests play a crucial part in regulating global climate change since their aboveground biomass (AGB) relates to the carbon cycle, and its changes affect the main carbon pools. At present, the most suitable available SAR data for wall-to-wall forest AGB estimation are exploiting an L-band polarimetric SAR. However, the saturation issues were reported for AGB estimation using L-band backscatter coefficients. Saturation varies depending on forest structure. Polarimetric information has the capability to identify different aspects of forest structure and therefore shows great potential for reducing saturation issues and improving estimation accuracy. In this study, 121 polarimetric decomposition observations, 10 polarimetric backscatter coefficients and their derived observations, and six texture features were extracted and applied for forest AGB estimation in a tropical forest and a boreal forest. A parametric feature optimization inversion model (Multiple linear stepwise regression, MSLR) and a nonparametric feature optimization inversion model (fast iterative procedure integrated into a K-nearest neighbor nonparameter algorithm, KNNFIFS) were used for polarimetric features optimization and forest AGB inversion. The results demonstrated the great potential of L-band polarimetric features for forest AGB estimation. KNNFIFS performed better both in tropical (R^2 = 0.80, RMSE = 22.55 Mg/ha, rRMSE = 14.59%, MA%E = 12.21%) and boreal (R^2 = 0.74, RMSE = 19.82 Mg/ha, rRMSE = 20.86%, MA%E = 20.19%) forests. Non-model-based polarimetric features performed better compared to features extracted by backscatter coefficients, model-based decompositions, and texture. Polarimetric observations also revealed site-dependent performances.

Keywords: forest AGB; polarimetric SAR observations; L-band; parametric and nonparametric feature optimization inversion methods

check for updates

Citation: Wang, M.; Zhang, W.; Ji, Y.; Marino, A.; Xu, K.; Zhao, L.; Shi, J.; Zhao, H. Aboveground Biomass Retrieval in Tropical and Boreal Forests Using L-Band Airborne Polarimetric Observations. *Forests* **2023**, *14*, 887. https://doi.org/10.3390/f14050887

Academic Editor: Jarosław Socha

Received: 13 March 2023
Revised: 15 April 2023
Accepted: 24 April 2023
Published: 26 April 2023

Copyright: © 2023 by the authors. Licensee MDPI, Basel, Switzerland. This article is an open access article distributed under the terms and conditions of the Creative Commons Attribution (CC BY) license (https://creativecommons.org/licenses/by/4.0/).

1. Introduction

Climate change is an obvious impact of the continuous development of human beings on Earth. Deforestation and forest degradation contributed to the continuous increase in global carbon dioxide (CO_2) and accelerated climate warming [1,2]. How to control and balance the carbon cycle has become a new central issue in the global response to climate change. Forests play a crucial part in regulating global climate change through mechanisms including carbon absorption, carbon emission, and the control of the water and energy cycles [3,4]. The main carbon pools are typically affected by the change in the living forest aboveground biomass (AGB). The current carbon stock in the world's forests is estimated at 861 ± 66 Pg C, where 471 ± 93 Pg C (55%) is stored in tropical forests and 272 ± 23 Pg C (32%) in boreal regions. The contribution of tropical and boreal forests to the carbon budget was 1.64 Pg C/year and 0.5 Pg C/year between 1990 and 2007, respectively [5–8]. Understanding the dynamics of tropical and boreal forests AGB changes is essential for comprehending the impact of forest management on climate change [1].

Therefore, accurate estimation of AGB in tropical and boreal forests is the key to reducing the uncertainty factor of carbon stock calculation, clarifying the potential of forest carbon sinks, and making sure the role of forests in the global carbon cycle [8]. AGB in tropical and boreal forests can be calculated with various methods. The destructive sampling through harvesting, drying, and weighting the living biomass is the most accurate way for AGB calculation [9,10]. National forest inventories over a wide area often carry out field measurements at permanent and temporary inventory plots and using allometric equations linking AGB to the diameter at breast height (DBH) and tree height [7–9,11–15]. However, ground surveys are time-consuming, expensive, and often impractical in both tropical and boreal forests with scarce accessibility. Remote sensing (RS) techniques have the advantage of monitoring forests at a large scale and have nowadays become the primary source for estimating AGB in tropical and boreal forests over large areas [9,11–15]. Landsat optical images were applied for AGB inversion both in tropical and boreal forests. The main limitation of optical images is the saturation at higher biomass values, resulting in high estimation errors for AGB. For example, the latest results of AGB estimation based on Landsat images revealed an accuracy of ±36% in the boreal zone [16,17]. Compared with optical sensors, Synthetic Aperture Radars (SARs) are expected to provide the most accurate AGB estimates since SARs are sensitive to vertical forest structures due to their deep penetration in canopies [18,19]. X-, C-, L-, and P-band SAR observations have been used for both tropical and boreal forests. P-band is expected to be the most suitable frequency for both tropical and boreal forest retrieval [20,21]. However, there is no current P-band SAR satellite mission, and this will only be available after the launch of BIOMASS. Additionally, it is harder to obtain high resolution at the P-band, and BIOMASS will not cover boreal regions in Europe and North America. Therefore L-band SAR will still play a key role in covering vast regions not covered by BIOMASS and providing higher resolution products, especially valuable for woodlands with lower AGB where P-band may have low sensitivity [8,22].

Japan Aerospace Exploration Agency (JAXA)'s Phased Array Type L-band Synthetic Aperture Radar (PALSAR) aboard the Advanced Land Observing Satellite (ALOS) and PALSAR-2 aboard ALOS-2 are widely used for forest AGB retrieval. Backscatter coefficients from HH, HV, and VV channels can be used for forest AGB inversion, where HV is demonstrated to have a high correlation to AGB [23,24]. However, the AGB estimates using L-band HV backscatter coefficients are valid up to a certain threshold where saturation occurs. The saturation point is approximately 75–150 mg/ha when using only the backscattering coefficient; the saturation point is where the slope of the AGB/L-band HV backscatter coefficient curve approaches zero [25]. To increase the saturation point, image texture, the ratio of polarimetric channels, interferometric coherence, and polarimetric features have been used. Those studies revealed that the saturation point could be increased to 200–300 Mg/ha. They also demonstrated that the saturation point depends on forest types which are influenced by forest structure [26–29].

Polarimetric information is sensitive to forest structure since the polarization of the scattered field is sensitive to the shape, orientation, and dielectric constant of forest scatterers [30]. However, the potential of polarimetric information at the L-band for improving forest AGB estimation is not fully understood due to the complexity of the inverse problem. Polarimetric target decompositions are a common method to analyze Polarimetric SAR (PolSAR) data. The principle is to decompose the complex scattering process from an object into several simpler scattering processes corresponding to single or partial scattering mechanisms [31]. Several target decomposition features were explored for AGB estimation. Features extracted from Freeman–Durden, Yamaguchi, and Cloude–Pottier decompositions were applied for forest growing stock volume (GSV) and forest AGB retrieval [30,32], reporting improvement in accuracy and saturation points at L-band [11,20]. However, with the introduction of new polarimetric decompositions, more and more polarimetric features could be extracted, and their potential need to be further explored.

Besides the selection of SAR features, the exploitation of suitable inversion algorithms is another crucial factor in obtaining precise AGB estimates [16,33]. Parametric and nonparametric algorithms have been used for AGB retrieval. With the abundance of more and more polarimetric decompositions, a large number of polarimetric SAR features are now available, leading to a need to improve parametric and nonparametric algorithms to have good mechanisms for selecting the optimal features. In this study, 137 polarimetric features extracted from L-band PolSAR images, including texture, backscatter coefficients, and polarimetric features (derived from 12 polarimetric decompositions), were applied in parametric and nonparametric feature optimization inversions (FOI) to explore the capability of L-band polarimetric observations for AGB inversion in tropical and boreal forests. The aim of this study is to fully explore the response of L-band polarimetric observations to forest AGB changes and the potential for inventories in tropical and boreal forests.

2. Materials and Methods

2.1. Test Site

Retrieval of forest AGB has been investigated in China at the tropical forest site of Diaoluo Mountain and in Sweden at the boreal forest site of Krycklan. At both sites, we have regular inventories. The ground measurements of forest variables are used to calculate AGB, which are then exploited to train models for AGB retrieval based on airborne PolSAR observations via a parametric and a nonparametric feature optimization inversion (FOI) algorithm.

The Diaoluo Mountain test site (18°0′ N, 109°41′ E; Figure 1a) is located in Hainan province of China. It is in a national forest park within the East Asian maritime tropical monsoon climate zone. Total precipitation per year ranges from 1870 mm to 2760 mm. The topography is fairly steep, with a ground elevation between 50 m and 1499 m above sea level. The forest types include tropical secondary, monsoon, and evergreen broadleaved forests with a coverage rate of 96.26%, in which coniferous mixed forest accounts for 73%. The understory of the forests is complex, dense, and full of foliage. The prevailing tree species are *Adinandra hainanensis* Hayata and *Dacrydium pectinatum* de Laubenfels.

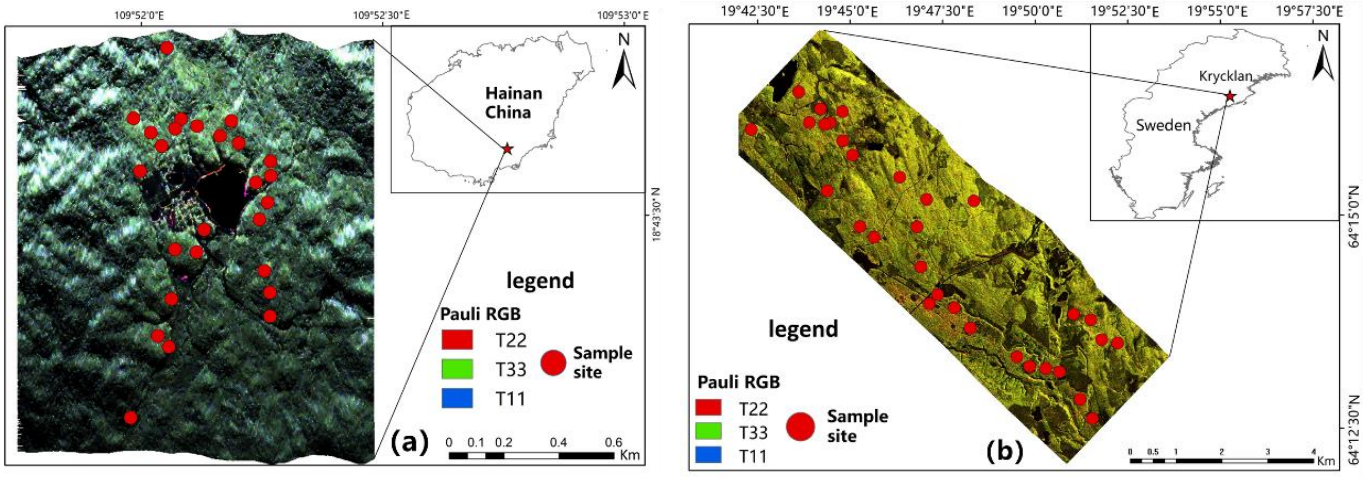

Figure 1. Hianan (**a**) and Sweden (**b**). Location map of the test site.

The Krycklan test site is located in northern Sweden (64°14′ N, 19°46′ E; Figure 1b). It is a watershed within the northern hemisphere's cold temperate zone. Topography is predominantly hilly with several gorges and elevation varies from 125 m to 350 m. The test site is rich in forest resources. The forest types include mixed coniferous and broad forests (72.8% coniferous), and the dominant species are Pinus sylvestris, *Picea abies*, and *Betula pubescens*. It is a naturally mature forest with a sparser stand of conical and spire-shaped canopies, fine cylindrical leaves, and a relatively clean understory.

2.2. Field Campaign

2.2.1. Diaoluo Mountain in Hainan Test Site

Systematic sampling was applied for field data collection at Diaoluo. It was conducted in April 2021. A total of 26 plots of 20 m × 20 m square plots (Figure 1a) were placed and investigated in the Diaoluo Mountain. The location of each plot was measured by real-time Kinematics (RTK) with an error less than 2 to 3 cm. Most of the plots are located on flat terrain with a maximum slope of 15 degrees.

The diameter at breast height (DBH), tree height of each tree with DBH greater than 3 cm were recorded. The AGB was calculated using the allometric equations published by Chave et al. [34]. Table 1 summarizes the allometric equations used in this study for five dominant tree species. The average wood density and the wood density of some tree species were referred to in the wood density table of major wood species in China. The species for which wood density could not be found were divided into four categories: soft broad, hard broad, pine, and fir, and the average wood density of each type was taken as their wood density. Figure 2a shows the AGB distribution of the 26 collected samples at Diaoluo. The AGB values ranged from 87.59 to 264.91 Mg/ha, the average DBH ranged from 9.38 to 11.54 cm, and the average tree height ranged from 6.93 to 10.44 m.

Table 1. Allometric equations for field collected forest AGB calculation in two test sites.

Test Site	Type	Allometric Equation	R^2
Hainan [34,35]	For DBH greater than 5 cm:	$AGB_{A\ tree} = 0.776 \cdot \left[\rho h (DBH)^2\right]^{0.94}$	0.969
	For DBH less than 5 cm:	$AGB_{A\ tree} = \rho/\rho_{ave} \exp[2.116 \ln(DBH) - 1.839]$	0.969
Sweden [36,37]	*Pinus sylvestris*	$AGB_{A\ tree} = b_0 + b_1 \cdot \ln(x_1) + b_2 \cdot \ln(x_2) + \cdots + \ln(\varepsilon)$	0.99
	Picea abies	$AGB_{A\ tree} = b_0 + b_1 \cdot \ln(x_1) + b_2 \cdot \ln(x_2) + \cdots + \ln(\varepsilon)$	0.99
	Betula pubescens	$AGB_{A\ tree} = b_0 + b_1 \cdot \ln(x_1) + b_2 \cdot \ln(x_2) + \cdots + \ln(\varepsilon)$	0.98

Note: Among these h is the height of the tree (m), ρ is the wood density (g/cm^{-3}), and ρ_{ave} is the average wood density (g/cm^{-3}), b_i are model parameters, x_i are independent variables, and $\ln(\varepsilon)$ is a random variable.

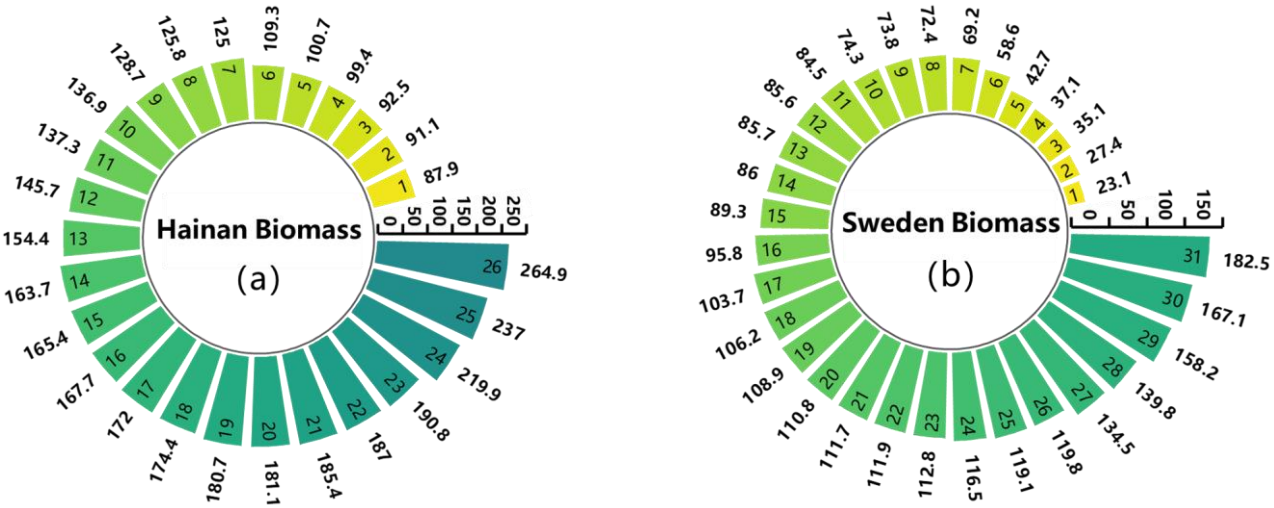

Figure 2. AGB details for the two test sites. The changes of each bar mean the increase in AGB values, the numbers on each bar of the circle represent the label of the plots, and the numbers out each bar of the circle represent the measured forest biomass (Mg/ha) of each plot.

2.2.2. Krycklan in Sweden Test Site

The field forest inventory at Krycklan site was carried out at the end of May 2007 during the BIOSAR II campaign. A total of 325 forest inventory plots with a radius of 10 m were measured in the whole test site. A total of 31 stands were randomly selected in this study. In the field campaign, trees with DBH greater than 4 cm are recorded,

unmeasured tree height and age are estimated through the Heureka system [36] (Heureka Wiki—Heureka Wiki (heurekaslu.se), https://www.heurekaslu.se/wiki/Heureka_Wiki, accessed on 5 January 2022.) for subsequent AGB calculation. The equations of anisotropic motion for the dominant tree species here have been published by Petersson in the Heureka system [37] and are given in Table 1. The AGB distribution of the selected 31 stands is shown in Figure 2b. Stand AGB ranged from 23.07 to 182.54 Mg/ha, mean DBH ranged from 8.65 to 58.84 cm, and mean tree height ranged from 7.5 to 21.4 m.

2.3. SAR Data Collection and Preprocessing

Airborne quad polarimetric SAR datasets were acquired in this study for two test sites, respectively. Details of the acquisitions are provided in Table 2.

Table 2. The detailed information of SAR data collected for the two test sites.

Parameter	Value (Hainan)	Value (Sweden)
Imaging time	2021-04	2008-10
polarization mode	HH, HV, VH, VV	HH, HV, VH, VV
Incidence angle/(°)	51.6	38.8
resolution (Range × Azimuth)/m	0.68 × 0.66	1.49 × 0.94

The preprocessing of the SAR data at the Hainan test site includes radiometric calibration, georeferencing and terrain correction, multi-looking, and Refine Lee speckle reduction filtering. In this study, the images acquired at Diaoluo Mountain were multi-looked with a multi-looking factor in range and azimuth of 2 × 2. Speckle noise in the images was reduced by applying Refine Lee filters with a moving window of 7 × 7 pixels. An external digital elevation model (DEM) derived from LiDAR point clouds dataset with 2 m resolution was used for SAR image geocoding and terrain correction. The terrain correction in this study includes three steps such as polarization orientation angle (POA) changes correction, effective scattering area (ESA) changes correction, and angular variation effect (AVE) correction [38].

According to [39], the preprocessing of images acquired in Sweden includes the generation of Raw product (Raw), Radar geometry image (RGI), and Geocoded and terrain-corrected product (GTC). After Raw and RGI, a single-look complex dataset is ready for geocoding and terrain correction. A 1 m resolution external DEM derived from LiDAR point cloud dataset was used in GTC procedure. For detailed information, readers are referred to [39].

2.4. SAR Features Extraction

In this study, 137 features were extracted from the quad polarimetric SAR acquisitions at each test site. The features are shown in Table 3. This includes backscatter coefficients, six indicators extracted from backscatter coefficients (including radar vegetation index (RVI), T11, T12, and T13 from T matrix, the total backscatter power Span and its dB version Span_db), and six texture indices. Finally, 137 features were derived from 14 polarimetric decompositions. The variables were extracted through polarimetric decompositions, including both model-based and non-model-based (here defined parametric). In Table 3, 137 extracted variables were divided into four groups such as backscatter-related, texture, non-model-based polarimetric features, and model-based polarimetric features for later AGB response analysis and retrieval.

Table 3. Four group of extracted polarimetric SAR observations for L-band SAR images.

Types	Number of Parameters	Polarimetric Attributes
Texture	6	Mean, homogeneity, entropy, dissimilarity, contrast, uniformity (Texture features extracted base on Gray-level Co-occurrence Matrix)
Model-based polarimetric features	24	R1 = Vol/(Odd + FDbl) (These components extracted from FreeMan3), R2 = Vol/(Odd+ Dbl + Hlx) (These components extracted from Yamaguchi4) [40] Vol and Ground features extracted from FreeMan2; Vol, Odd, Dbl features extracted from VanZyl3; An_Yang3, FreeMan3 and Yamaguchi3, respectively [41,42]. Vol, Odd, Dbl, Hlx features extracted from An_Yang4_ Yamaguchi4 [43].
Backscatter related	10	HH, HV, VH, VV, T11, T22, T33, RVI, Span, Span_db
Non-model-based Polarimetric features	97	Entropy, HA ((1−Entropy)(1−Anisotropy)), 1 Mha(Entropy (1−Anisotropy)), H1 mA (Entropy * Anisotropy), 1 mH1 mA ((1−Entropy) Anisotropy), Pedestal Height, Shannon Entropy, polarization fraction Anisotropy12, Eigenvalues Relative Diffrernce, Polarization Asymmetry, Lueneburg Anisotropy, Alpha, beta, delta, gamma, lambda, Anisotropy, Eigenvalues, Pseudo Probabililties, Anisotropy, Shannon Index, Inverse Simpson Index, Gini Simpson, Index, Reyni Entropy, Index of Qualitative Inversion (IQV), Simpson Index, Perplexity [31] Kd (Helix scattering), ks (Sphere scattering), and kh (Dihedral scattering) features extracted from Krogager decomposition method Tau (Helix scattering), delta_ph (Plane scattering), delta_pha (Multiple scattering), psi (Scattering angle) feature extracted from Neumann decomposition M_S1, M_S2, M_S3, Phip_S1, Phip_S2, Phip_S3, Tawp_mean, Tawp_S1, Tawp_S2, Tawp_S3, Alphap_mean, Alphap_S1, Alphap_S2, Alphap_S3, Phip_mean, Orientation_max_mean, Orientation_max_S2, Orientation_max_S3 features extracted from Aghababaee decomposition [44] alpha_s, alpha_s1, alpha_s2, alpha_s3, phi_s, phi_s1, phi_s2, phi_s3, psi_s, psi_s1, psi_s2, psi_s3, tau_s, tau_s1, tau_s2, tau_s3 features extracted from TSVM decomposition [45]

Note: These features are named as *1_*2, *1 is the decomposition method name and *2 is the name of features, for example Aghababaee_M_S1. Vol, Odd, Dbl are volume scattering mechanism, surface scattering mechanism, and double bounce scattering mechanism, respectively; Span is total backscattered power; M_S1, M_S2, M_S3 are three maximum amplitude return value; Phip_S1, Phip_S2, Phip_S3 are four target phase angle parameters; Tawp_mean, Tawp_S1, Tawp_S2, Tawp_S3 are four 4 target ellipticity angle parameters; Alphap_mean, Alphap_S1, Alphap_S2, Alphap_S3 are four symmetry scattering parameters.

2.5. Inversion Method

Using the measured forest AGB as the dependent (response) variable and SAR observations derived from the L-band as the independent (predictor) variables, the forest AGB was retrieved for the two test sites based on a multiple linear stepwise regression (MSLR) models and a fast iterative feature selection for K-nearest neighbor (KNNFIFS) algorithm. A leave-one-out cross-validation method was used for validating the retrieved forest AGB [46].

2.5.1. MSLR Model

Multiple linear stepwise regression (MSLR) is widely used in remote sensing forest AGB estimation. It is a linear method to predict forest AGB assuming a linear relationship between the dependent and independent variables. Stepwise regression evaluates input SAR features step by step, adding and eliminating variables based on their significance. It not only improves the accuracy of AGB estimation but also solves the problem of high dimensionality and high covariance resulting from small samples and highly collinear variables. The basic idea of MSLR is to introduce the feature parameters into the model one by one, conduct a significance test for each introduced feature parameter, retain the significant feature parameters, and reject the original feature parameters if the introduced new feature makes the original feature parameters becoming no longer significant. An optimal model is obtained until the model does not introduce new feature parameters nor reject the original feature parameters. However, since forest AGB is related to many

factors, such as canopy structure, tree density, and tree species composition, the relationship between it and the SAR features is often too complex to be well interpreted by a linear function.

2.5.2. KNNFIFS Model

In this study, a fast iterative procedure was integrated into a K-nearest neighbor nonparameter algorithm for optimal SAR observations selection and forest AGB estimation. The method is named the KNNFIFS algorithm; it has been used in previous research and performed well in forest AGB estimation [12]. The four key steps are included in KNNFIFS: Step1: the definition of initial dataset according to SAR observations and number of field-collected plots. This is defined as $F = \{f_1, f_2, \cdots, f_m\}$, where m describes the number of selected initial SAR variables and $f_j = [x_{j1}, x_{j2}, \cdots, x_{jn}]^T (1 \leq j \leq m)$. x_{ji} is the pixel value of the *jth* SAR feature at the *ith* plot, where n is the plot number. Step2: initialization of the initial best optimal SAR feature subset and the initial value of root means square error (RMSE) of the ideal KNN model according to the maximum AGB values of the test site. The initial best optimal SAR feature subset is set as $F_s = \{null\}$, $s = 0$, where s is the number of selected optimal SAR observations. Step3: KNN model generation and validation. $m - s$ KNN models and their retrieval RMSE values by feature combinations of $\{f_1, F_s\}, \{f_2, F_s\}, \cdots, \{f_{i-1}, F_s\}, \{f_{i+1}, F_s\}, \cdots,$ and $\{f_m, F_s\}$ were generated and validated, where $f_i = F_s \cap F$ and the RMSE values were calculated with the leave one out cross-validation (LOOCV) method. Step4: derivation of best KNN models, optimal SAR feature subset, and best forest AGB retrieval result. The lowest value of RMSE calculated in Step3 is set as $RMSE_b$; if $RMSE_b < RMSE_0$, then $RMSE_0 = RMSE_b$ and the feature combination for the $RMSE_0$ is set for F_s. Step3 is repeated until $RMSE_b \geq RMSE_0$. The flow chart of KNNFIFS algorithm and the four key steps are shown in Figure 3.

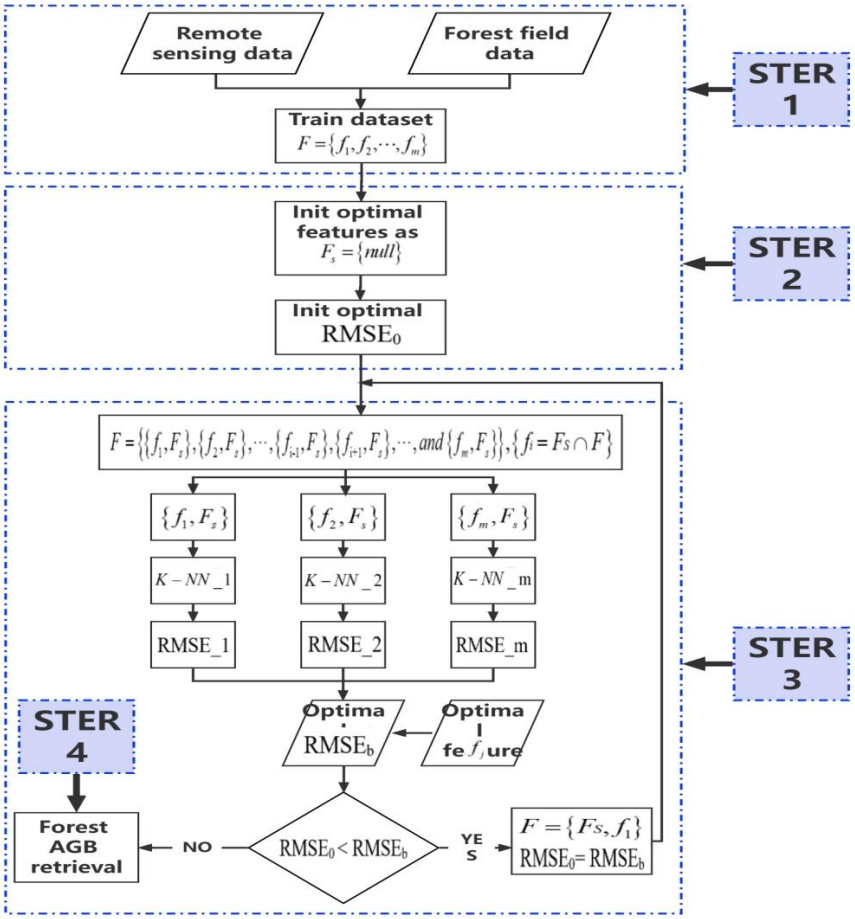

Figure 3. Flow chart of KNNFIFS algorithm.

2.5.3. Forest AGB Estimation and Validation

The coefficient of determination (R^2, Equation (1)), root mean square error (RMSE, Mg/ha, Equation (2)), relative error (rRMSE, %, Equation (3)), and mean absolute percentage (MA%E, %, Equation (4)) are used. R^2 represents the accuracy of the model and ranges from 0 to 1, with values closer to 1 representing greater accuracy. The RMSE measures the difference between predicted and measured values, with a smaller value indicating greater accuracy. MA%E and rRMSE represent the magnitude and percentage of deviation between predicted and measured values, with smaller values indicating less deviation from the model.

$$R^2 = 1 - \frac{\sum_{i-1}^{n}(Y_i - y_i)^2}{\sum_{i-1}^{n}(Y_i - \overline{y})^2} \quad (1)$$

$$RMSE = \sqrt{\frac{\sum_{i-1}^{n}(Y_i - y_i)^2}{n}} \quad (2)$$

$$\text{rRMSE} = \frac{RMSE}{\overline{y}} \times 100\% \quad (3)$$

$$\text{MA\%E} = \frac{1}{n}\sum_{i=1}^{n}\left|\frac{Y_i - y_i}{Y_i}\right| \times 100\% \quad (4)$$

where Y_i is the measured forest AGB value of the ith sample plot, y_i is the forest AGB estimated value of the with sample plot, $\overline{y}$ is the mean of the measured forest biomass. n is the number of sample plots.

3. Result

We divided the forest AGB values of the two test sites into nine groups: A (representing the AGB at the level of 20~49 Mg/ha), B (50~79 Mg/ha), C (80~109 Mg/ha), D (110~129 Mg/ha), E (130~159 Mg/ha), F (160~189 Mg/ha), G (190~209 Mg/ha), H (210~239 Mg/ha), and I (240~270 Mg/ha). Among the best SAR features selected by MSLR and KNNFIFS, those with a more sensitive response to changes in forest AGB are plotted here in Figure 4 by the corresponding L-band extracted feature values for each biomass class in order to illustrate how SAR observations correlate with the level of forest AGB. In order to quantify the relationships between each SAR observation and forest AGB, Pearson's correlation coefficient (r) was calculated and shown in each subplot. To better understand the performance of MSLR and KNNFIFS at two test sites for forest AGB retrieval, we graphed the AGB retrieved using MSLR and KNNFIFS against ground measurements in scatter plots. All of the features as input and features divided into four different categories in Table 3 as input of the two inversion algorithms were performed at two test sites here. The scatter plots for their performance analysis are shown in Figures 5–7.

3.1. Analysis of L-Band Polarimetric Observations' Sensitivity to Forest AGB

The evolution of the selected optimal L-band polarimetric observable was analyzed as a function of the AGB through nine different levels. Their trends were compared at two test sites with the objective of interpreting the forest scattering mechanisms at the L-band. Figure 4 revealed that the sensitivity of polarimetric SAR features to forest AGB showed obvious site dependence.

In the Hainan test site, we observed low correlations between the four backscatter coefficients and AGB, with r values ranging from 0.07 and 0.11. Nevertheless, the HV polarization channel, which usually represents the scattering from randomly oriented volumes, correlates best to forest AGB among the four channels. Meanwhile, the radar vegetation index (RVI), which provides information on the stochasticity of natural targets, showed higher sensitivity to AGB when compared with the four polarization channels. In the Sweden test site, the backscatter values at the four polarization channels were

significantly correlated with the forest AGB at 0.01 confidence level, and the correlation coefficients of the VV channel to forest AGB is the highest with r = 0.584. Next are HH and HV, with r = 0.5. All the four-polarization backscatter coefficients increased with the increase in forest AGB. The highest correlation shown by VV may result from vertical orientation features and needs to be further studied. In this study area, forest cover is sparser, which resulted in larger penetration and multiple reflection effects [46].

Comparing the L-band backscatter values of the two experimental fields with different changes in response to forest AGB, after relative calibration, the dynamic range in Sweden's backscatter values is between −4 and −6 dB, whereas Hanan backscatter values are between −10 and −24 dB. However, this temperate coniferous test site, with straight trunks and sparse canopies, provides the ideal conditions for SAR signals to penetrate deep in the canopy and multiple reflect on the trunks and ground. In contrast, the Hanan experimental site is characterized by dense and highly depressed tropical evergreen broadleaf forests with a greater number of plants between layers. Since the echo signal weakens after the microwave penetrates the rainforest, the sensitivity to the high biomass tropical rainforest is low [47]. When analyzing scattering from vegetation zones, RVI uses a medium cylinder model with randomly pointing medium cylinders.

Model-based decompositions also show obvious site dependence. The features extracted in Sweden correlate better to forest AGB than that extracted at Hainan. In the Hainan test site, the volume scattering (Vol) in the three decomposition methods (i.e., Freeman, An_Yang, and Yamaguchi) shows some correlation to AGB, while the rest of the features are uncorrelated to AGB. However, in the Sweden test site, volume scattering (Vol) derived from the three decompositions have higher correlation coefficients (r = 0.526, r = 0.494, and r = 0.447, respectively). On the other hand, the double bounce scattering mechanism (Dbl) and surface scattering (Odd) show lower sensitivity to AGB compared with Vol. This corroborates the fact that VV is not correlated because of the ground or double bounce; it may be an orientation of the volume in the canopy.

The non-model-based polarimetric decompositions show higher correlations with AGB over the Hainan test site, thanks to their characteristic focus on different and adaptive scattering mechanisms. Features include the target randomness parameter (anisotropy_lueneburg with r = 0.39), Shannon_entropy (r = −0.713), scattering angle (alpha with r = 0.251), and helical scattering component of Neumann decomposition (Neumann_tau with r = 0.355). anisotropy_lueneburg may capture the randomness of forest canopies or underwood in Hainan [48]. Shannon_entropy includes the intensity (SEI) and the degree of polarization (SEP). It shows the capability to represent the complexity of scattering mechanisms in forest structures [49]. The good correlation of Neumann_tau (which describes a helical scattering mechanism) also seems to represent the complexity of the forest structure resulting in non-reflection symmetric targets. Anisotropy and alpha3 were weakly sensitive to changes in forest AGB, while gamma was highly sensitive to changes in forest AGB in the range of 110–290 Mg/ha. SE was mainly affected by total backscattering; the higher the forest AGB, the lower the value of SE, and therefore the sensitivity of SE to forest AGB was high and reached a significant negative correlation at the 0.01 level. In the Sweden test site, Shannon_entropy also correlates well with forest AGB change with r = 0.584. However, features showing a high correlation with AGB at Hainan show no obvious correlation with AGB in Sweden. Note that the evolution of Aghaba-baee_Phip_S1 and Aghababaee_M_S1 showed a similar trend with Vol features in the target polarimetric decomposition method and then has a high correlation with forest AGB (r = 0.423 and r = 0.607, respectively). TSVM decomposition was reported to perform well in AGB retrieval in tropical forest biomass [50]. Compared with TSVM decomposition, Aghababaee decomposition considers asymmetric scattering, making the contribution of asymmetric scattering in forest regions more reasonable [51]. In Hainan, features extracted from TSVM and Aghababaee have a weak correlation with forest AGB. Although several features from Aghababee decomposition correlated better with forest AGB in Sweden, the features derived from TSVM showed no obvious correlation with forest AGB.

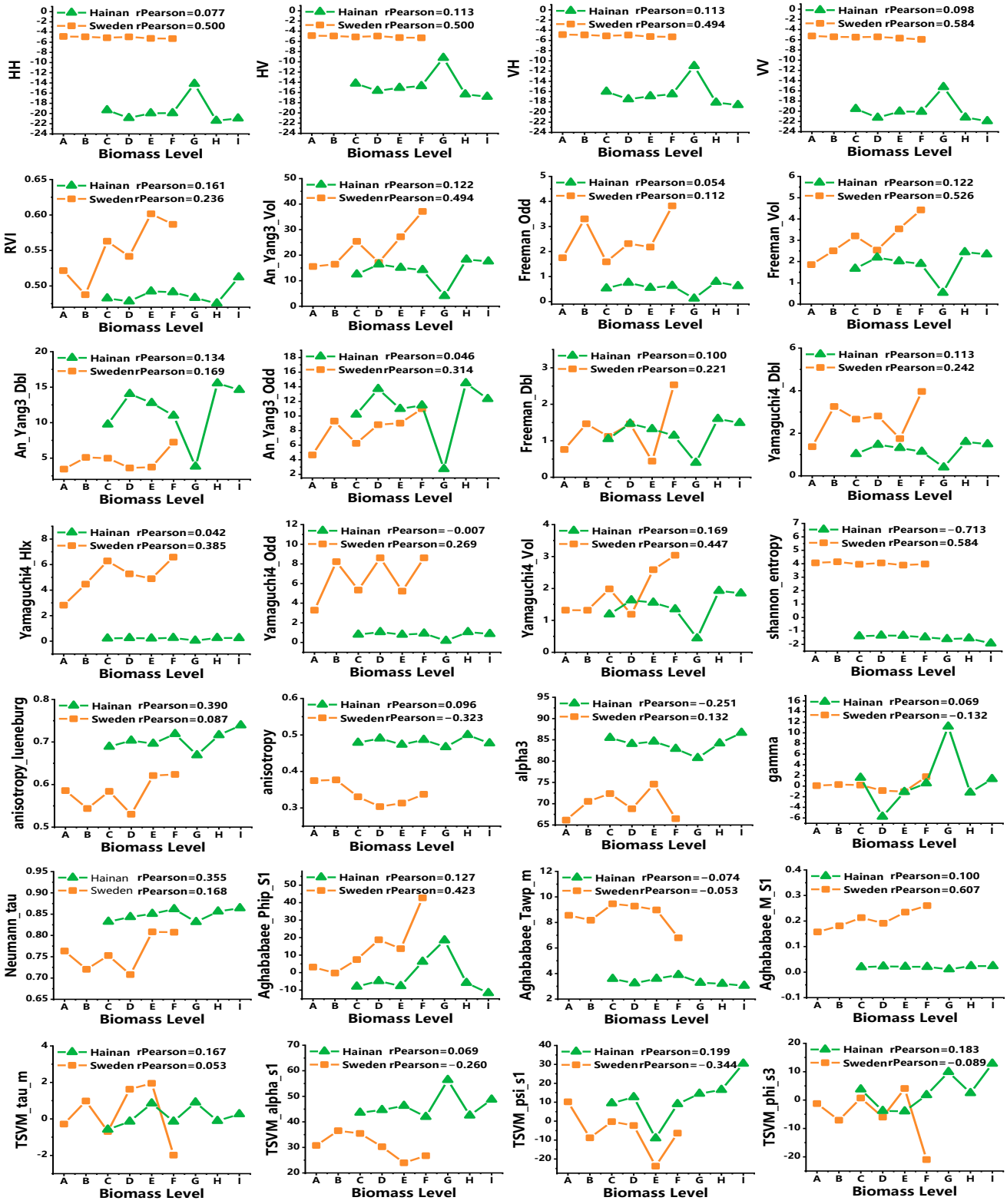

Figure 4. Response of L-band polarimetric SAR observations to forest AGB. (The unit of biomass is Mg/ha; the r values between SAR features and AGB were calculated through SPASS software).

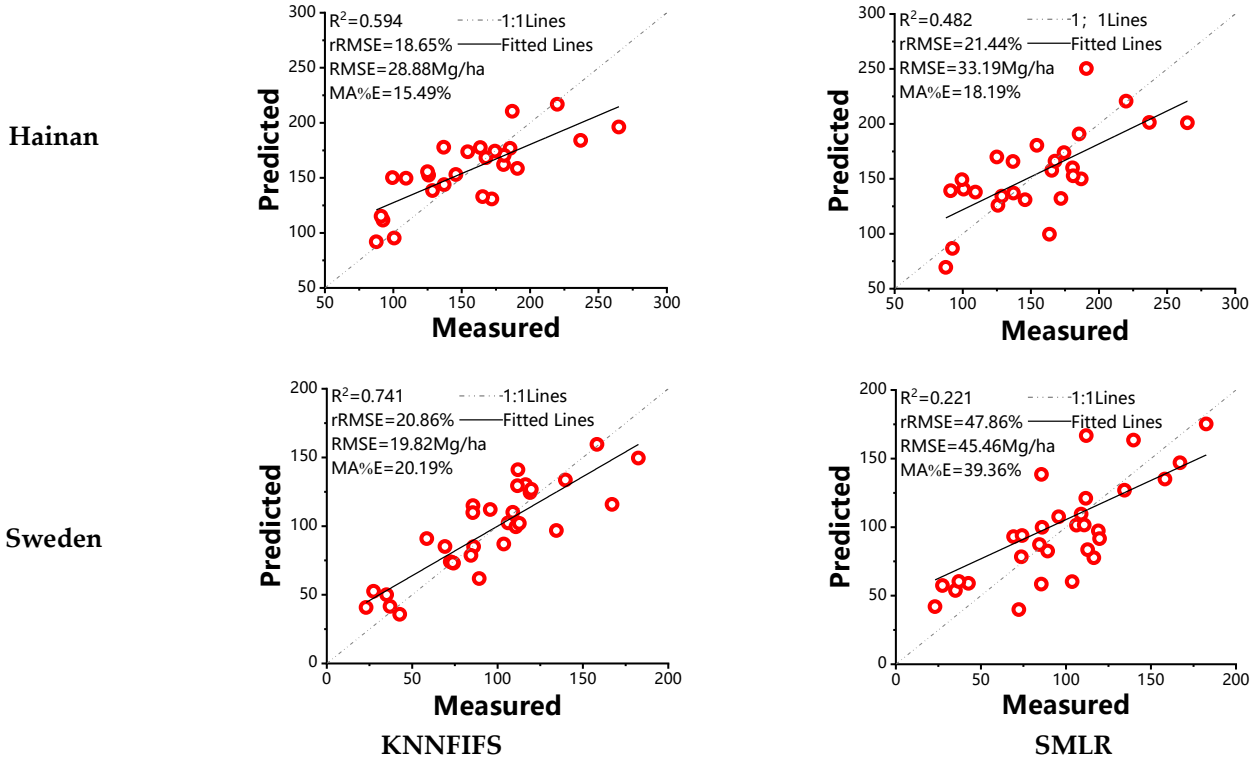

Figure 5. Forest AGB estimation using SMLR and KNN-FIFS at Hainan and Sweden test sites.

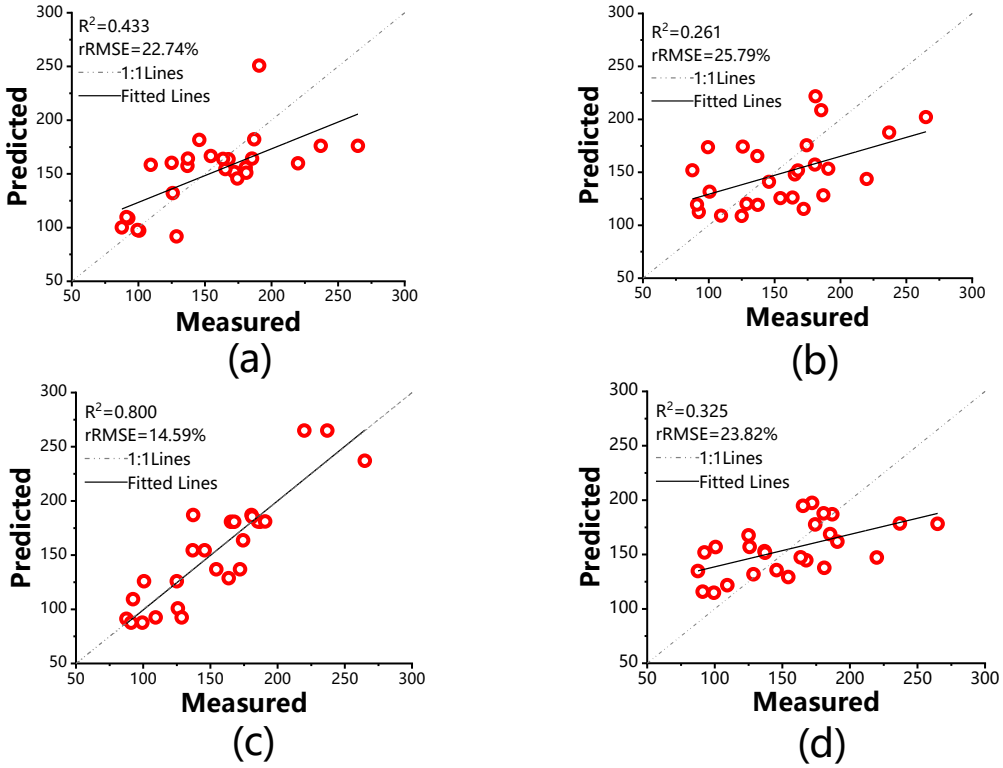

Figure 6. Forest AGB estimation using KNNFIFS at Hainan using four polarimetric SAR feature groups: (**a**) Backscatter related features; (**b**) Texture; (**c**) Polarimetric features; (**d**) Model-based polarimetric features.

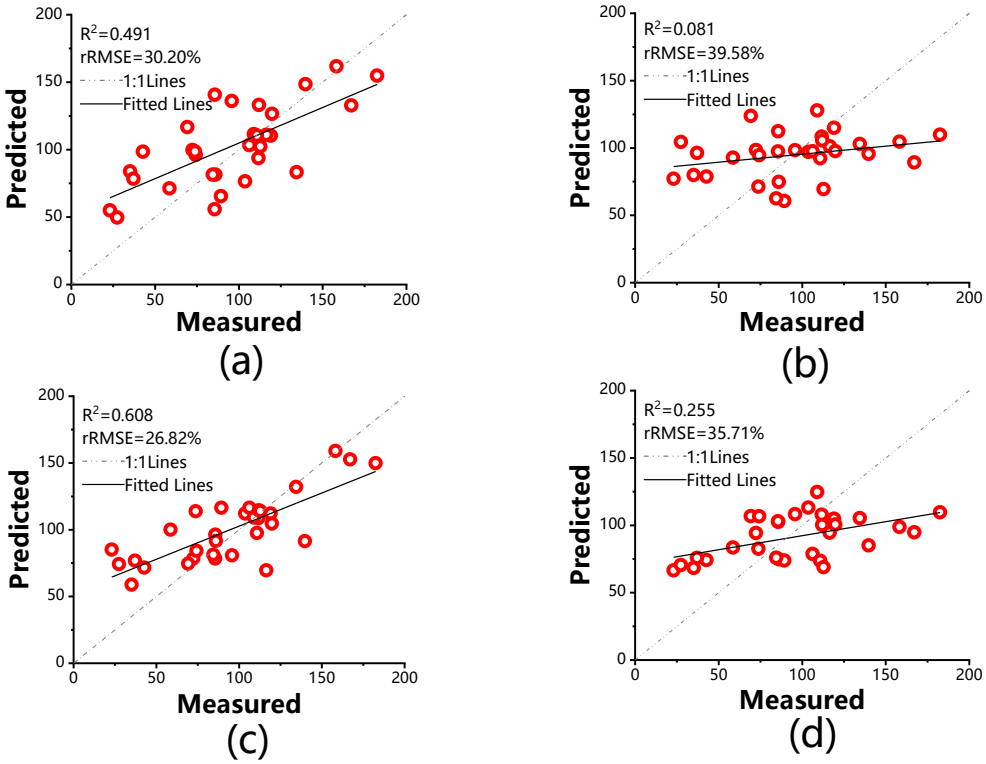

Figure 7. Forest AGB estimation using KNNFIFS at Sweden using four polarimetric SAR feature groups: (**a**) Backscatter related features; (**b**) Texture; (**c**) Polarimetric features; (**d**) Model-based polarimetric features.

Polarimetric features that have high correlation coefficients regarding AGB differ from site to site, which reveals that features extracted from different polarimetric decompositions show different sensitivity in response to various forest scattering mechanisms. The complex tropical forest scene and the higher forest AGB level in Hainan made it difficult to measure AGB with L-band backscatter coefficients and regular polarimetric features. However, the sparser boreal forest scene with lower forest AGB level and clean underwood in Sweden improved the retrieval when using L-band backscatter coefficients and regular polarimetric features.

3.2. Forest AGB Estimation

The forest AGBs were retrieved by SMLR and KNNFIFS algorithm for two test sites. The results of the two models were compared. Figure 5 plots the estimated results against ground-measured samples. KNNFIFS performed better at both test sites than SMLR, showing that linear models may not capture the relationships well. In Hainan, the R^2 value is 0.594, and the RMSE values are 28.88 Mg/ha with rRMSE = 18.65% and MA%E = 15.49%. Although the R^2 = 0.741 is the highest in Sweden, the RMSE value is 19.82 Mg/ha. When looking at the rRMSE = 20.86%, we notice a worse result than in Hainan. This is possibly because values in Hainan are larger, having more AGB.

SMLR seems to show a poor fit to real AGB in Figure 5. The scatter plots revealed a serious overestimation of low AGB and an underestimation of high AGB when using the SMLR algorithm, especially at the Krycklan test site. The results confirm the effectiveness of KNNFIFS with L-band SAR polarimetric data for AGB retrieval at different test sites.

In order to further explore the potential of L-band polarimetric SAR for forest AGB estimation, we built models using four different feature groups in Table 3. Figures 6 and 7 show the scatter plots of AGB estimation using each feature group at the two test sites, respectively. Tables 4 and 5 summarize the parameters of KNNFIFS models and also the related R^2, RMSE, rRMSE, and MA%E values.

Table 4. Statistics of forest AGB estimate derived from KNNFIFS model using four SAR feature groups at Hainan test site.

SAR Feature Group	K	Window Size	R^2	RMSE	rRMSE	MA%E
Backscatter features	2	5	0.433	34.30	22.74%	16.59%
Texture features	3	11	0.261	39.93	25.79%	23.10%
Non-model-based Polarimetric features	1	3	0.800	22.55	14.59%	12.21%
Model-based polarimetric features	6	3	0.325	36.93	23.82%	20.57%

Note: K represents the number of nearest neighbors, and a window represents the size of the window in which SAR feature information is extracted.

Table 5. Statistics of forest AGB estimate derived from KNNFIFS model using 4 SAR feature groups at Sweden test site.

SAR Feature Group	K	Window Size	R^2	RMSE	rRMSE	MA%E
Backscatter features	3	5	0.491	28.69	30.20%	36.88%
Texture features	8	5	0.081	37.60	39.58%	48.89%
Polarimetric features	3	9	0.608	25.48	26.82%	34.57%
Model-based polarimetric features	11	3	0.225	33.92	35.71%	40.60%

Note: K represents the number of nearest neighbors, and a window represents the size of the window in which SAR feature information is extracted.

Each feature group shows different retrieval performances in Hainan and Sweden. According to Tables 4 and 5, for non-model-based polarimetric features, the relative RMSE at Hainan and Sweden was 14.56% and 26.82%, respectively. This feature group performed best in both test sites. However, the retrieval error for Hainan was, on average, about 5% over using the entire set of SAR features, whereas, for Sweden, it was about 5% lower, which also confirmed the forest structure effects on the inversion results. Next, better retrieval performance was returned by the backscatter features resulting in rRMSEs of 20%–30%, RMSEs of 20–30 Mg/ha, R^2 of 0.4–0.5, and MA%E of 15%–35%. Compared with the best performance in each test site, in the case of Hainan, the rRMSE decreased by about 20%, and RMSE increased by about 10 Mg/ha; in the case of Sweden to 8% and 10 Mg/ha for rRMSE and RMSE, respectively. The retrieval with texture features and model-based polarimetric features provides a further decrease when compared to the estimates using whole SAR features. Meanwhile, they showed the same retrieval performance in two test sites. The retrieval from model-based polarimetric features performed better than texture features. For model-based polarimetric features, the relative RMSE at Hainan and Sweden was 23.82% and 35.71%, respectively. For texture features, the relative RMSE at Hainan and Sweden was 25.79% and 39.58%, respectively.

Figures 6 and 7 illustrated the relationships between real AGB and estimated AGB for four retrieval scenarios (four group SAR features) at two test sites. The fitted line and agreement line (1:1 line) are shown in each scatterplot. In Figure 6c, the fitted line and agreement line are almost overlapping, and there is no obvious saturation phenomenon. It revealed the great potential of polarimetric features for forest AGB estimation in tropical forests. In other subplots in Figure 6, underestimation of high values and overestimation of low values occurred after the forest AGB was greater than 100 Mg/ha. A clear saturation phenomenon also is visible in these scatterplots. In Figure 7, in line with what was observed in Figure 6a,b,d, we found the underestimation of high values and overestimation of low values occurred in each subplot. Although in Figure 7a,c, backscatter features, and polarimetric features showed the availability of these SAR observations for the retrieval of forest AGB, AGB values lower than 50 Mg/ha are greatly overestimated, and AGB values greater than 100 Mg/ha are greatly underestimated. In Figure 7b,d, the predicted AGB dynamic range becomes narrow and only around 100 Mg/ha and reveals the weak sensitivity of texture features and model-based polarimetric features to forest AGB.

The estimation using polarization decompositions matches well with the in situ AGB, but there is an underestimation of the forest AGB level before 100 Mg/ha. With

backscattering coefficients, there is a large underestimation of forest AGB in the range of 100–125 Mg/ha. Model-based decompositions and texture features show severe underestimation and overestimation, especially the texture features with saturation after an AGB of 50 Mg/ha.

Table 6 summarizes the best KNNFIFS models and their optimal selected SAR features for the two test sites. In Hainan, the best performance is obtained using only polarimetric features, while in Sweden, it is obtained by all features as input to the model.

Table 6. Best inversion models and their optimal features and model parameter at two test sites.

Test Site	R^2	K	Window Size	KNNFIF SPreferred Characteristic Parameters
Hainan	0.800	1	3	TSVM_Psi3, shannon_entropy, Aghababaee_Tawp_m, Aghababaee_M1, reyni_entropy3, pedestal, gamma, TSVM_tau_m
Sweden	0.741	2	3	VV, Aghababaee_Tawp_m, TSVM_tau_m, R2

Note: K represents the number of nearest neighbors, and a window represents the size of the window in which SAR feature information can be extracted.

4. Discussion and Conclusions

The forest AGB retrieval performance using 137 L-band polarimetric observations by SMLR and KNNFIFS was assessed with the aid of forest inventory plots at two test sites. KNNFIFS performed better in forest AGB retrieval in two test sites with R^2 = 0.800 and R^2 = 0.741, respectively. To better understand the performance of the selected two algorithms in this study, we retrieved the forest AGB using K-nearest nearest neighbor (KNN) and random forest (RF) at the two test sites using all of the 137 SAR polarimetric observations (Table 7). Table 7 summarizes the estimated results in the two test sites. KNN performed better than RF both in two test sites with lower rRMSE values, but the R^2 between the retrieved AGB and the field measurements in Sweden is the lowest, and the value is 0.054. The worse performance of RF may result from too many input SAR observations without the removal of those that appeared in multiple decision trees in RF. Compared with RF, KNN performed better in forests with more complex forest structures. The results coincided with our previous study [33].

Table 7. The results obtained by RF and KNN at two test sites.

Test Site	Methods	R^2	RMSE (Mg/ha)	rRMSE (%)
Hainan	RF	0.257	64.96	41.97
	KNN	0.373	37.86	24.46
Sweden	RF	0.248	68.65	44.35
	KNN	0.298	33.03	34.78

In the literature, L-band polarimetric features extracted from Freeman–Durden, Yamaguchi, and Cloude–Pottier decompositions have shown to be useful to forest classification and retrieval of forest bio-physical parameters as tree height, forest stand age, and forest growing stock volume (GSV). The study of Gonçalves et al. [47] using airborne L-band polarimetric SAR data showed the correlation of all of the scattering mechanisms to the GSV but did not show the physical significance of the observed trend. Kobayashi et al. [32] extended [47] and found canopy scattering and surface scattering have a high correlation with GSV and forest height, but double bounce scattering showed almost no correlation with these forest biometric parameters. Previous studies showed Span (r = 0.51) and entropy (r = 0.56) from model-based polarimetric features had more significant correlations with forest AGB [48]. Traditional forest AGB estimates based on L-band SAR backscatter show signal saturation between 75 and 150 Mg/ha, whereas the addition of time series data results in no signal saturation below 280 Mg/ha [49]. Features extracted from TSVM decomposition correlate well with forest AGB with r = 0.554 and r = −0.689 in Yiliang and Genhe test sites in our previous study [50]. In contrast, not all of the correlation coefficients

of the extracted polarimetric features used in this study show higher values when compared with previous studies. However, most of them were confirmed to have a correlation with forest AGB with a significance level of 1%. Since forest structure and tree species affect polarimetric decomposition parameters, it is possible that different polarimetric features show sensitivity to different forest types [30,51,52]. This study also confirms a clear forest structure-dependency of the 137 polarimetric observables used.

As a consequence of the site-specific relationship between polarimetric SAR observations and forest AGB, the accuracy of the retrieved forest AGB differs at the two test sites when using different combinations of extracted polarimetric SAR features. It is important to optimize the selection of suitable SAR observables to improve AGB estimation according to the characteristics of the forest. At Hainan, the strongest agreement was obtained by polarimetric features (Figure 6c); the scatter plots of in situ and retrieved AGB presented a high agreement with $R^2 = 0.80$. Differently than at Hainan, the performance of polarimetric SAR observations in Sweden improved when the whole 137 polarimetric features worked as model feature input. Previous studies on the optimization of remote sensing features in forest AGB estimation also demonstrated the necessity for selecting suitable RS features for improving forest AGB estimation accuracy [11,12,16]. Santoro et al. [14] and Cartus et al. [21] also demonstrated that the features and models trained by one type of forest but used for other types of forest AGB estimation did not perform equally well and advised that features and models should be made adaptive to the forest structure to avoid biases in the retrieved forest AGB or GSV. Moreover, the results of both this study and Tuong's study showed that in some conditions, forest AGB estimates based on polarization features were not significantly saturated; Tuong et al. [53] effectively estimated forest AGB above 240 Mg/ha, and in this study, we were able to effectively estimate forests above 260 Mg/ha. It meant the method used in this study has the potential to improve the accuracy and saturation of forest AGB inversions.

The results show that KNNFIFS are more accurate than SMLR featuring higher coefficients of determination and lower RMSEs at the two test sites. A similarly fast iterative procedure embedded in KNN applied in AGB estimation of different forest types using different remote sensing features also demonstrated the robustness and transferability of the KNNFIFS algorithm. Using a water cloud model, Santoro estimated the trunk volume of boreal forest with an RMSE of 30%–40%; Cartus et al. estimated the AGB of tropical and boreal forests using a water cloud model and backscatter coefficients with relative errors of around 20%–40% [14,20,21]. Although previous studies demonstrated it is valuable to compare the performance of retrieval algorithms, they also recognized the uncertainties resulting from remote sensing observation differences were important [15,54]. Moreover, since the different test sites covered different forest types with different forest structures and AGB levels, it is really difficult to compare various algorithms, especially using different satellite data acquired with different modes [11,55–57].

In summary, the results show that KNNFIFS performed better than the MSLR model for forest AGB estimation. They also confirmed that the KNNFIFS algorithm is transferable and still provides appropriate AGB estimations validation at different test sites and using different input features. The results generally confirmed the site dependence of forest AGB estimation using polarimetric features. They also revealed the distinguished capability of polarimetric features for AGB retrieval. L-band SAR polarimetric observations allow for estimating AGB with a relative error of 20%–30%. In both test sites, the best performance showed no obvious saturation point. Although the good performance of L-band polarimetric observations with KNNFIFS algorithms in two test sites, there are overfit phenomena of KNNFIFS algorithms during forest AGB retrieval procedures, and the reason for the improvement in the performance of the algorithm needs to be further explored. Moreover, since there is a limitation of acquired L-band images at two test sites and limited in situ samples, in the future, with an abundance of acquisition plans of existing or planned spaceborne L-band (e.g., NiSAR, ALOS-2/4) missions, suitable L-band polarimetric features at boreal and tropical forests should be further explored.

Author Contributions: Conceptualization, W.Z.; methodology, M.W.; project administration, W.Z.; resources, W.Z.; software, M.W., K.X., L.Z. and J.S.; supervision, W.Z. and Y.J.; validation, M.W. and J.S.; writing—original draft preparation, M.W. and W.Z.; writing—review and editing, W.Z., A.M. and Y.J.; visualization, M.W., J.S. and H.Z. All authors have read and agreed to the published version of the manuscript.

Funding: The research was supported by National Natural Science Foundation of China (Grant No. 32160365, 42161059 and 31860240) and the Agriculture joint special project of Yunnan province (Grant No. 202301BD070001-058).

Data Availability Statement: The datasets analyzed during the current study are available from the Institute of Forest Resources Information Technique, Chinese Academy of Forestry, but restrictions apply to the availability of these data and so they are not publicly available.

Acknowledgments: The authors would like to thank the European Space Agency (https://www.esa.int/, accessed on 11 January 2022) for providing the Polarimetric SAR Data Processing and Educational Toolbox (PolSARpro) software for effectively manipulating the SAR data. Part of this work was performed under the support of China scholarship Council (CSC). The authors are grateful to Zongtao Han of Weihai Wuzhou Navi-Tech for providing the KNNFIFS model.

Conflicts of Interest: The authors declare no conflict of interest.

References

1. Qin, Y.; Xiao, X.; Wigneron, J.-P.; Ciais, P.; Canadell, J.G.; Brandt, M.; Li, X.; Fan, L.; Wu, X.; Tang, H.; et al. Large Loss and Rapid Recovery of Vegetation Cover and Aboveground Biomass over Forest Areas in Australia during 2019–2020. *Remote Sens. Environ.* **2022**, *278*, 113087. [CrossRef]
2. Achard, F.; Eva, H.D.; Mayaux, P.; Stibig, H.-J.; Belward, A. Improved Estimates of Net Carbon Emissions from Land Cover Change in the Tropics for the 1990s. *Glob. Biogeochem. Cycles* **2004**, *18*, 1–11. [CrossRef]
3. Herold, M.; Carter, S.; Avitabile, V.; Espejo, A.B.; Jonckheere, I.; Lucas, R.; McRoberts, R.E.; Næsset, E.; Nightingale, J.; Petersen, R.; et al. The Role and Need for Space-Based Forest Biomass-Related Measurements in Environmental Management and Policy. *Surv. Geophys.* **2019**, *40*, 757–778. [CrossRef]
4. Puliti, S.; Breidenbach, J.; Schumacher, J.; Hauglin, M.; Klingenberg, T.F.; Astrup, R. Above-Ground Biomass Change Estimation Using National Forest Inventory Data with Sentinel-2 and Landsat. *Remote Sens. Environ.* **2021**, *265*, 112644. [CrossRef]
5. Cochrane, M.A. *Tropical Fire Ecology Climate Change, Land Use and Ecosystem Dynamics*; Springer: Berlin/Heidelberg, Germany, 2009; ISBN 978-3-540-77381-8.
6. Pan, Y.; Birdsey, R.A.; Fang, J.; Houghton, R.; Kauppi, P.E.; Kurz, W.A.; Phillips, O.L.; Shvidenko, A.; Lewis, S.L.; Canadell, J.G.; et al. A Large and Persistent Carbon Sink in the World's Forests. *Science* **2011**, *333*, 988–993. [CrossRef]
7. Santoro, M.; Cartus, O.; Fransson, J.E.S. Dynamics of the Swedish Forest Carbon Pool between 2010 and 2015 Estimated from Satellite L-Band SAR Observations. *Remote Sens. Environ.* **2022**, *270*, 112846. [CrossRef]
8. Le Toan, T.; Quegan, S.; Davidson, M.W.J.; Balzter, H.; Paillou, P.; Papathanassiou, K.; Plummer, S.; Rocca, F.; Saatchi, S.; Shugart, H.; et al. The BIOMASS Mission: Mapping Global Forest Biomass to Better Understand the Terrestrial Carbon Cycle. *Remote Sens. Environ.* **2011**, *115*, 2850–2860. [CrossRef]
9. Goetz, S.J.; Baccini, A.; Laporte, N.T.; Johns, T.; Walker, W.; Kellndorfer, J.; Houghton, R.A.; Sun, M. Mapping and Monitoring Carbon Stocks with Satellite Observations: A Comparison of Methods. *Carbon Balance Manag.* **2009**, *4*, 2. [CrossRef]
10. Nordh, N.; Verwijst, T. Above-Ground Biomass Assessments and First Cutting Cycle Production in Willow (*Salix* Sp.) Coppice—A Comparison between Destructive and Non-Destructive Methods. *Biomass Bioenergy* **2004**, *27*, 1–8. [CrossRef]
11. Ji, Y.; Xu, K.; Zeng, P.; Zhang, W. GA-SVR Algorithm for Improving Forest Above Ground Biomass Estimation Using SAR Data. *IEEE J. Sel. Top. Appl. Earth Obs. Remote Sens.* **2021**, *14*, 6585–6595. [CrossRef]
12. Han, Z.; Jiang, H.; Wang, W. Forest Above-Ground Biomass Estimation Using KNN-FIFS Method Based on Multi-Source Remote Sensing Data. *Sci. Silvae Sin.* **2018**, *54*, 70–79. [CrossRef]
13. PAN, J.; XING, Y.; HUANG, J. Estimation of Forest Above-Ground Biomass Based on GF-3 PolSAR Data and Landsat-8 OLI Data. *J. Cent. South Univ. For. Technol.* **2020**, *40*, 83–90. [CrossRef]
14. Santoro, M.; Cartus, O.; Fransson, J.E.S.; Wegmüller, U. Complementarity of X-, C-, and L-Band SAR Backscatter Observations to Retrieve Forest Stem Volume in Boreal Forest. *Remote Sens.* **2019**, *11*, 1563. [CrossRef]
15. Englhart, S.; Keuck, V.; Siegert, F. Modeling Aboveground Biomass in Tropical Forests Using Multi-Frequency SAR Data—A Comparison of Methods. *IEEE J. Sel. Top. Appl. Earth Obs. Remote Sens.* **2012**, *5*, 298–306. [CrossRef]
16. Lu, D.; Chen, Q.; Wang, G.; Liu, L.; Li, G.; Moran, E. A Survey of Remote Sensing-Based Aboveground Biomass Estimation Methods in Forest Ecosystems. *Int. J. Digit. Earth* **2016**, *9*, 63–105. [CrossRef]
17. Ji, L.; Wylie, B.K.; Nossov, D.R. Estimating Aboveground Biomass in Interior Alaska with Landsat Data and Field Measurements. *Int. J. Appl. Earth Obs. Geoinf.* **2012**, *18*, 451–461. [CrossRef]

18. Le Toan, T.; Beaudoin, A.; Riom, J.; Guyon, D. Relating Forest Biomass to SAR Data. *IEEE Trans. Geosci. Remote Sens.* **1992**, *30*, 403–411. [CrossRef]
19. Bispo, P.C.; Santos, J.R.; Valeriano, M.M.; Touzi, R.; Seifert, F.M. Integration of Polarimetric PALSAR Attributes and Local Geomorphometric Variables Derived from SRTM for Forest Biomass Modeling in Central Amazonia. *Can. J. Remote Sens.* **2014**, *40*, 26–42. [CrossRef]
20. Cartus, O.; Santoro, M. Exploring Combinations of Multi-Temporal and Multi-Frequency Radar Backscatter Observations to Estimate above-Ground Biomass of Tropical Forest. *Remote Sens. Environ.* **2019**, *232*, 111313. [CrossRef]
21. Cartus, O.; Santoro, M.; Wegmüller, U.; Rommen, B. Benchmarking the Retrieval of Biomass in Boreal Forests Using P-Band SAR Backscatter with Multi-Temporal C- and L-Band Observations. *Remote Sens.* **2019**, *11*, 1695. [CrossRef]
22. Sandberg, G.; Ulander, L.M.H.; Fransson, J.E.S.; Holmgren, J.; Le Toan, T. L- and P-Band Backscatter Intensity for Biomass Retrieval in Hemiboreal Forest. *Remote Sens. Environ.* **2011**, *115*, 2874–2886. [CrossRef]
23. Sinha, S.; Jeganathan, C.; Sharma, L.K.; Nathawat, M.S. A Review of Radar Remote Sensing for Biomass Estimation. *Int. J. Environ. Sci. Technol.* **2015**, *12*, 1779–1792. [CrossRef]
24. Villard, L.; Le Toan, T.; Ho Tong Minh, D.; Mermoz, S.; Bouvet, A. Forest Biomass from Radar Remote Sensing. In *Land Surface Remote Sensing in Agriculture and Forest*; Elsevier: Amsterdam, The Netherlands, 2016; pp. 363–425, ISBN 978-1-78548-103-1.
25. Englhart, S.; Keuck, V.; Siegert, F. Aboveground Biomass Retrieval in Tropical Forests—The Potential of Combined X- and L-Band SAR Data Use. *Remote Sens. Environ.* **2011**, *115*, 1260–1271. [CrossRef]
26. Mermoz, S.; Le Toan, T.; Villard, L.; Réjou-Méchain, M.; Seifert-Granzin, J. Biomass Assessment in the Cameroon Savanna Using ALOS PALSAR Data. *Remote Sens. Environ.* **2014**, *155*, 109–119. [CrossRef]
27. Yu, Y.; Saatchi, S. Sensitivity of L-Band SAR Backscatter to Aboveground Biomass of Global Forests. *Remote Sens.* **2016**, *8*, 522. [CrossRef]
28. Cartus, O.; Santoro, M.; Kellndorfer, J. Mapping Forest Aboveground Biomass in the Northeastern United States with ALOS PALSAR Dual-Polarization L-Band. *Remote Sens. Environ.* **2012**, *124*, 466–478. [CrossRef]
29. Thapa, R.B.; Watanabe, M.; Motohka, T.; Shimada, M. Potential of High-Resolution ALOS–PALSAR Mosaic Texture for Aboveground Forest Carbon Tracking in Tropical Region. *Remote Sens. Environ.* **2015**, *160*, 122–133. [CrossRef]
30. Chowdhury, T.; Thiel, C.; Schmullius, C.; Stelmaszczuk-Górska, M. Polarimetric Parameters for Growing Stock Volume Estimation Using ALOS PALSAR L-Band Data over Siberian Forests. *Remote Sens.* **2013**, *5*, 5725–5756. [CrossRef]
31. Lee, J.-S.; Eric, P. *Polarimetric Radar Imaging: From Basics to Applications*; CRC Press: Boca Raton, FL, USA, 2013; ISBN 978-1-4200-5497-2.
32. Kobayashi, S.; Omura, Y.; Sanga-Ngoie, K.; Widyorini, R.; Kawai, S.; Supriadi, B.; Yamaguchi, Y. Characteristics of Decomposition Powers of L-Band Multi-Polarimetric SAR in Assessing Tree Growth of Industrial Plantation Forests in the Tropics. *Remote Sens.* **2012**, *4*, 3058–3077. [CrossRef]
33. Zhang, W.; Zhao, L.; Li, Y.; Shi, J.; Yan, M.; Ji, Y. Forest Above-Ground Biomass Inversion Using Optical and SAR Images Based on a Multi-Step Feature Optimized Inversion Model. *Remote Sens.* **2022**, *14*, 1608. [CrossRef]
34. Chave, J.; Andalo, C.; Brown, S.; Cairns, M.A.; Chambers, J.Q.; Eamus, D.; Fölster, H.; Fromard, F.; Higuchi, N.; Kira, T.; et al. Tree Allometry and Improved Estimation of Carbon Stocks and Balance in Tropical Forests. *Oecologia* **2005**, *145*, 87–99. [CrossRef] [PubMed]
35. Shao, X.; Cheng, Y.; Wang, X. Distribution Patterns of Aboveground Biomass of Tropical Cloud Forests in Hainan Island. *Chin. J. Ecol.* **2022**, *37*, 2566–2572. [CrossRef]
36. Heureka Heureka Wiki—Heureka Wiki (Heurekaslu.Se). Available online: https://www.heurekaslu.se/wiki/Heureka_Wiki (accessed on 5 January 2022).
37. Petersson, H. *Biomassafunktioner För Trädfaktorer Av Tall, Gran Och Björk i Sverige*; Arbetsrapport; Sveriges Lantbruksuniversitet, Institutionen för Skoglig Resurshushållning och Geomatik: Uppsala, Sweden, 1999; pp. 2–31.
38. Zhao, L.; Chen, E.; Li, Z.; Zhang, W.; Gu, X. Three-Step Semi-Empirical Radiometric Terrain Correction Approach for PolSAR Data Applied to Forested Areas. *Remote Sens.* **2017**, *9*, 269. [CrossRef]
39. *BioSAR 2008 Technical Assistance for the Development of Airborne SAR and Geophysical Measurements during the BioSAR 2008 Experiment: Draft Final Report—BioSAR Campaign*; ESA Contract No. 22052/08/NL/CT; European Space Agency: Paris, France; German Aerospace Center DLR: Cologne, Germany; Swedish Defence Research Agency (FOI): Stockholm, Sweden, 2009; pp. 3–138.
40. Wei, J.; Fan, W.; Yu, Y.; Mao, X. Polarimetric Decomposition Parameters for Artificial Forest Canopy Biomass Estimation Using GF-3 Fully Polarimetric SAR Data. *Sci. Silvae Sin.* **2020**, *56*, 174–183. [CrossRef]
41. An, W.; Cui, Y.; Yang, J. Three-Component Model-Based Decomposition for Polarimetric SAR Data. *IEEE Trans. Geosci. Remote Sens.* **2010**, *48*, 2732–2739. [CrossRef]
42. Freeman, A.; Durden, S.L. A Three-Component Scattering Model for Polarimetric SAR Data. *IEEE Trans. Geosci. Remote Sens.* **1998**, *36*, 963–973. [CrossRef]
43. Yamaguchi, Y.; Moriyama, T.; Ishido, M.; Yamada, H. Four-Component Scattering Model for Polarimetric SAR Image Decomposition. *IEEE Trans. Geosci. Remote Sens.* **2005**, *43*, 1699–1706. [CrossRef]
44. Aghababaee, H.; Sahebi, M.R. Incoherent Target Scattering Decomposition of Polarimetric SAR Data Based on Vector Model Roll-Invariant Parameters. *IEEE Trans. Geosci. Remote Sens.* **2016**, *54*, 4392–4401. [CrossRef]
45. Touzi, R. Target Scattering Decomposition in Terms of Roll-Invariant Target Parameters. *IEEE Trans. Geosci. Remote Sens.* **2007**, *45*, 73–84. [CrossRef]

46. Breiman, L. Heuristics of Instability and Stabilization in Model Selection. *Ann. Stat.* **1996**, *24*, 2350–2383. [CrossRef]
47. Gonçalves, F.G.; Santos, J.R.; Treuhaft, R.N. Stem Volume of Tropical Forests from Polarimetric Radar. *Int. J. Remote Sens.* **2011**, *32*, 503–522. [CrossRef]
48. Neumann, M.; Saatchi, S.S.; Ulander, L.M.H.; Fransson, J.E.S. Assessing Performance of L- and P-Band Polarimetric Interferometric SAR Data in Estimating Boreal Forest Above-Ground Biomass. *IEEE Trans. Geosci. Remote Sens.* **2012**, *50*, 714–726. [CrossRef]
49. Hayashi, M.; Motohka, T.; Sawada, Y. Aboveground Biomass Mapping Using ALOS-2/PALSAR-2 Time-Series Images for Borneo's Forest. *IEEE J. Sel. Top. Appl. Earth Obs. Remote Sens.* **2019**, *12*, 5167–5177. [CrossRef]
50. Zeng, P.; Zhang, W.; Li, Y.; Shi, J.; Wang, Z. Forest Total and Component Above-Ground Biomass (AGB) Estimation through C- and L-Band Polarimetric SAR Data. *Forests* **2022**, *13*, 442. [CrossRef]
51. Watanabe, M.; Shimada, M.; Rosenqvist, A.; Tadono, T.; Matsuoka, M.; Romshoo, S.A.; Ohta, K.; Furuta, R.; Nakamura, K.; Moriyama, T. Forest Structure Dependency of the Relation Between L-Band Σ0 and Biophysical Parameters. *IEEE Trans. Geosci. Remote Sens.* **2006**, *44*, 3154–3165. [CrossRef]
52. Jon Ranson, K.; Sun, G. An Evaluation of AIRSAR and SIR-C/X-SAR Images for Mapping Northern Forest Attributes in Maine, USA. *Remote Sens. Environ.* **1997**, *59*, 203–222. [CrossRef]
53. Tuong, T.; Tani, H.; Wang, X.; Thang, N.; Bui, H. Combination of SAR Polarimetric Parametersfor Estimating Tropical ForestAbove-ground Biomass. *Pol. J. Environ. Stud.* **2020**, *29*, 3353–3365. [CrossRef]
54. Gao, Y.; Lu, D.; Li, G.; Wang, G.; Chen, Q.; Liu, L.; Li, D. Comparative Analysis of Modeling Algorithms for Forest Aboveground Biomass Estimation in a Subtropical Region. *Remote Sens.* **2018**, *10*, 627. [CrossRef]
55. Saatchi, S.; Marlier, M.; Chazdon, R.L.; Clark, D.B.; Russell, A.E. Impact of Spatial Variability of Tropical Forest Structure on Radar Estimation of Aboveground Biomass. *Remote Sens. Environ.* **2011**, *115*, 2836–2849. [CrossRef]
56. Ji, Y.; Huang, J.; Ju, Y.; Guo, S.; Yue, C. Forest Structure Dependency Analysis of L-Band SAR Backscatter. *PeerJ* **2020**, *8*, e10055. [CrossRef]
57. Lu, D. The Potential and Challenge of Remote Sensing-based Biomass Estimation. *Int. J. Remote Sens.* **2006**, *27*, 1297–1328. [CrossRef]

Disclaimer/Publisher's Note: The statements, opinions and data contained in all publications are solely those of the individual author(s) and contributor(s) and not of MDPI and/or the editor(s). MDPI and/or the editor(s) disclaim responsibility for any injury to people or property resulting from any ideas, methods, instructions or products referred to in the content.